J Adv Ceram

Research Article

An aluminum surface modification strategy for enhancing CMAS corrosion resistance of environmental barrier coatings

Lin Dong[1], Chen-Ze Bai[1], Mei-Jun Liu[1,✉], Guan-Jun Yang[1,✉], Wen-Jing Wang[1], Xiao-Feng Zhang[2], Ke-Song Zhou[2]

Cite this article: Dong L, Bai C-Z, Liu M-J, et al. *J Adv Ceram* 2026, **15**(2): 9221222. https://doi.org/10.26599/JAC.2025.9221222

ABSTRACT: As the inlet temperature of engines increases, injected sand, volcanic ash, and dust melt to form calcium–magnesium–aluminosilicate (CMAS) glass, which subsequently adheres to the surface of ytterbium monosilicate (YbMS; Yb_2SiO_5) environmental barrier coatings (EBCs), posing a serious degradation threat. In this study, a novel aluminum surface modification strategy was proposed to prevent direct interaction between the coatings and CMAS, thereby increasing corrosion resistance. The modification confers a dual-protection mechanism: First, it seals exposed interconnections deposited by air plasma spray (APS) and facilitates the *in situ* formation of a dense, continuous ytterbium aluminum garnet (YbAG; $Yb_3Al_5O_{12}$) layer, serving as the primary, nonreactive physical barrier against CMAS infiltration; second, it inhibits silica consumption by YbMS while releasing silica into the melt. This process increases the melt viscosity, fundamentally suppressing CMAS penetration. The combined effect of these mechanisms extends the coating life by at least 10 times. Although the CMAS resistance of unmodified YbMS is inferior to that of previous ytterbium disilicate (YbDS; $Yb_2Si_2O_7$) coatings, aluminum-modified YbMS has significantly greater resistance than modified YbDS. This performance reversal is attributed to the unique microstructure of YbMS, which favors the formation of a higher-quality, more protective YbAG layer, thereby fundamentally altering the CMAS interaction mechanism.

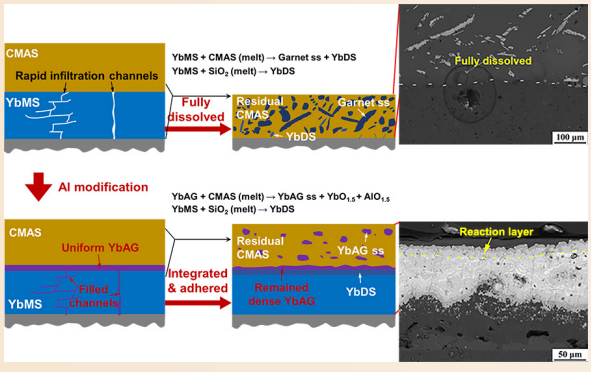

KEYWORDS: environmental barrier coatings (EBCs); calcium–magnesium–aluminosilicate (CMAS); corrosion resistance; densification; surface modification

1 Introduction

Silicon carbon ceramic matrix composites (SiC-CMCs) are transforming aerospace turbines by enabling engines to operate at higher temperatures and efficiencies than ever before. Their outstanding properties—high-temperature strength, lightweight structure, oxidation resistance, and fatigue resistance—make them ideal for high-pressure turbine blades, vanes, and shrouds. Nevertheless, SiC-CMCs are highly susceptible to water vapor degradation, which leads to severe silica volatilization and material deterioration. To address this challenge, environmental barrier coatings (EBCs) are essential for protecting SiC-CMC components from harsh combustion environments, ensuring their long-term durability and reliability in aerospace turbine applications. By preventing oxidation and corrosion, EBCs play a crucial role in enhancing the efficiency and lifespan of modern aircraft engines [1,2].

As the operating temperatures of new-generation turbines continue to increase, molten salt degradation poses a significant threat to EBC materials. At elevated temperatures, injected sand, volcanic dashes, and dust melt and form calcium–magnesium–aluminosilicate (CMAS) glass, which adheres to the coatings. The molten CMAS reacts with the EBC materials, leading to their gradual recession and degradation. To ensure long-term performance and reliability, developing materials with high resistance to CMAS infiltration and degradation is crucial.

Rare-earth (RE) silicates, particularly ytterbium silicates, are considered the most promising topcoat materials because of their high thermal stability, excellent resistance to water vapor corrosion, and coefficient of thermal expansion (CTE) comparable to that of SiC (ytterbium silicates (4–7)×10^6 K^{-1} [1–3], SiC (4.5–5.5)×10^6 K^{-1} [1]). Unlike thermal barrier coatings (TBCs), which mainly fail due to mechanical delamination, dense EBCs degrade predominantly through chemical corrosion in the presence of CMAS [4–6]. Ytterbium monosilicate (YbMS;

[1] State Key Laboratory for Mechanical Behavior of Materials, School of Materials Science and Engineering, Xi'an Jiaotong University, Xi'an 710049, China.
[2] National Engineering Laboratory for Modern Materials Surface Engineering Technology, Guangdong Academy of Science, Guangzhou 510650, China.
✉ Corresponding authors. E-mail: M.-J. Liu, liumjun@mail.xjtu.edu.cn; G.-J. Yang, ygj@mail.xjtu.edu.cn

Received: July 15, 2025; Revised: November 13, 2025; Accepted: November 28, 2025

Yb_2SiO_5) and ytterbium disilicate (YbDS; $Yb_2Si_2O_7$) readily react with CMAS to generate reaction products such as $Ca_2Yb_8(SiO)_6O_2$ apatite [3], $CaAl_2Si_2O_8$ anorthite [7], and garnet [1,8]. Several studies have reported different degrees of CMAS-induced degradation. Jang *et al.* [9] reported that after reacting at 1400 °C for 48 h, an apatite reaction layer with a thickness of approximately 120 μm formed in YbMS. Abrar *et al.* [10] fabricated a high-entropy RE monosilicate (MS) dense bulk material and detected a recession thickness of 30–35 μm after reacting at 1300 °C for 48 h. Turcer *et al.* [11] reported that CMAS completely infiltrated into YbDS pellets after reacting at 1500 °C for 24 h, causing a thickness dilatation gradient and severe blistering and cracking. Liu *et al.* [12] investigated the corrosion of YbMS/YbDS/Si trilayer EBCs at different temperatures for up to 50 h and demonstrated that YbMS exhibited better stability in molten CMAS than did YbDS because of its more stable crystal structure. However, Zhao *et al.* [13] reported that YbDS showed better CMAS resistance than YbMS at 1300 °C, as it consumed more CMAS to form apatite, thus effectively slowing degradation. These studies indicate that CMAS corrosion behavior is significantly dependent on temperature, exposure time, and material composition.

The CMAS corrosion mechanism is highly complex and influenced by many factors, including the melt composition, exposure temperature, and melt load. A higher Ca:Si ratio increases the likelihood of crystallized apatite formation at the CMAS/coating interface but also reduces melt viscosity and accelerates grain boundary penetration [14–16]. Elevated temperatures further increase the reaction activation energy and melt viscosity, enhancing the chemical reactions between the EBC materials and the molten CMAS, disrupting the integrity of the reaction layer, and accelerating coating degradation [17]. Additionally, the CMAS load plays a crucial role in determining failure modes. Under moderate-to-heavy CMAS loads, coating degradation is typically driven by material dissolution and reprecipitation. However, under low melt exposure, the coating experienced different failure modes due to reduced coating dissolution and the lack of a continuous apatite layer at the melt/coating interface, making it vulnerable to unrestricted melt infiltration [18]. In summary, melt infiltration and coating recession, driven by material dissolution and reprecipitation, are the predominant failure mechanisms of CMAS-exposed EBCs.

Many researchers believe that incorporating thermoreacted secondary phases of CMAS and EBC materials as coating materials can help prevent melt penetration. Since garnet exhibits strong corrosion resistance to CMAS, significant effort has been put into promoting its formation on coating surfaces. Silicate oxyapatite $Ca_2Y_8(SiO_4)_6O_2$ is considered a potential EBC material because it can effectively resist the chemical corrosion of CMAS below 1300 °C and form a cyclosilicate layer at the CMAS/apatite interface [19]. Additionally, the introduction of iron to stabilize yttrium has been shown to promote the formation of yttrium aluminum garnet (YAG; $Y_3Al_5O_{12}$) on MS coatings, thereby effectively inhibiting CMAS infiltration [20]. Compared with apatite, garnet exhibits superior CMAS resistance because of its greater consumption of melt constituents and reduced reliance on RE elements [21–23]. The $Y_3Al_5O_{12}$ garnet/Al_2O_3 eutectic ceramic bulk has a CMAS corrosion layer thickness of < 40.58 μm after 32 h of corrosion at 1300 °C, which is far lower than the corrosion depth of conventional coatings (200–375 μm for yttria-stabilized zirconia (YSZ)-based coatings [24]). Previously, our group [25,26] proposed a postdensification method, which involves infiltrating aluminum into the surface-exposed pores and microcracks of the YbDS coating to form a thin ytterbium aluminum garnet (YbAG; $Yb_3Al_5O_{12}$) layer on the surface, which serves as an effective barrier against oxidation and corrosion. The corrosion thickness of the modified coating was reduced by 90% (from 15.2 to 3.5 μm at 1300 °C; from 19 to 4.2 μm at 1400 °C), and it remained intact even after 25 h of corrosion at 1400 °C. However, under these conditions, the unmodified YbDS completely dissolved [26]. The diffusion and direct interaction of corrosives are restricted, thereby significantly enhancing corrosion resistance.

This study investigated the aluminum modification of YbMS/mullite/Si trilayer coatings, focusing on their high-temperature interactions with CMAS, microstructural evolution, and corrosion resistance mechanisms. Additionally, the corrosion performance of these YbMS coatings was compared with that of previously developed YbDS systems. The underlying mechanisms leading to the performance differences were investigated in depth through calculations related to atomic-scale reactions, surface absorption, and crystal stability. These findings provide broader insights into molten salt corrosion mechanisms and offer valuable inspiration for the microstructural design of EBCs to mitigate CMAS-induced degradation.

2 Experimental

2.1 Coating preparation

The YbMS/mullite/Si trilayer coatings were fabricated via a commercial air plasma spray (APS) system (GP-80, Jiu-jiang, China) on SiC wafers (ϕ25.4 mm × 3 mm), which were preheated at approximately 200 °C. The deposition parameters of each layer are listed in Table 1. For the top coat, agglomerated YbMS powders were used, prepared via solid synthesis and spray-drying, with a particle size range of 15–60 μm. The interlayer and bond layers were deposited using crushed mullite and Si powders, respectively, both with a size distribution of 10–40 μm.

The modification process consists of two steps: pressure-assisted infiltration followed by heat treatment. In the first step, a 3–5 μm thick aluminum film was deposited onto the sprayed coating surface using a vacuum magnetron sputtering system (J-1250, Jingzhou Industrial Coating, China), which is a well-known method for depositing thin, highly uniform and dense metallic films on a rough APS coating surface. The coated samples were then pressure infiltrated in a furnace at 750 °C under a 100 kPa Ar atmosphere (O_2 < 0.001 ppm) to achieve densification. In the second step, the infiltrated samples were heated at 1100 °C for 2 h in an Ar atmosphere (O_2 < 0.001 ppm) to promote the *in situ* reaction between aluminum and YbMS, with a heating and cooling rate of 5 °C·min^{-1}. The detailed parameters of the modification process can be found in our previous studies [24–26]. The as-sprayed YbMS/mullite/Si trilayer coating is designated the MS coating, whereas the aluminum-modified coating is referred to as the aluminum-monosilicate (Al-MS) coating. The fabrication and corrosion performance of the reference disilicate (DS) and aluminum-disilicate (Al-DS) coatings used here for comparative analysis have been reported previously [26] and were adopted directly from that study.

2.2 CMAS corrosion

In this study, natural vermiculite silicate was employed as a CMAS material to represent the fly ash commonly ingested by aero engines. Its molar composition was determined to be $49SiO_2$–3CaO–37MgO–$11AlO_{1.5}$. The powder was first dispersed in ethanol and then uniformly applied on the coating surface repeatedly until the average loading density reached

approximately 40 mg·cm^{-2}. The CMAS-coated samples were then placed into a box furnace and subjected to the following heat treatment: heated to 1100 °C at a rate of 10 °C·min^{-1}; further heated to 1400 °C at a rate of 5 °C·min^{-1}; held for 1, 5, 25, or 50 h; and finally cooled to ambient temperature at a rate of 10 °C·min^{-1} inside the furnace.

2.3 Characterizations

The melting points and reaction temperatures of CMAS and CMAS/YbMS mixtures (1:1 wt%) were determined via a thermogravimetric analysis-differential scanning calorimeter (TG-DSC; STA449F3, NETZSCH, Germany) under an Ar atmosphere, with a heating rate of 10 °C·min^{-1} up to 1400 °C. The surface phase compositions of the coatings were identified through X-ray diffraction (XRD) in a 2θ configuration from 10° to 90°, followed by analysis via Jade software and the PDS database. Microstructural characterization of the coatings was performed by a scanning electron microscope (SEM; MIRA 3 LMH, Tescan, the Czech Republic). The phase composition and elemental distribution were analyzed via an energy dispersive spectroscope (EDS; AZTEC, Oxford Instruments, UK) equipped with SEM. For microscopic structural and crystalline phase characterization, the coatings were further analyzed via a transmission electron microscope (TEM; JEM-F200, JEOL, Japan). High-resolution TEM (HRTEM), EDS, and selected area diffraction (SEAD) images were collected. The TEM samples were fabricated via a focused ion beam (FIB; Helios Nanolab 600i, FEI, USA) system. Digital micrograph software was used to analyze the spectrograms.

The coating thickness was determined via the area measurement method detailed in our previous work [26]. The measurement was performed via five SEM images of each sample. The corrosion thickness was evaluated by subtracting the residual thickness from the initial value. First-principle calculations were performed to determine the bond energies of the crystals. The crystal structures were built with Materials Studio software and then processed via the Vienna *Ab initio* Simulation Package (VASP). Electron exchange and correlation were treated with the projector augmented wave (PAW) method and the generalized gradient approximation (GGA) of Perdew, Burke, and Ernzerhof (PBE). We used a plane-wave basis set with a cutoff energy of 420 eV and sampled the Brillouin zone with a 4 × 4 × 4 *k*-point mesh. All the structures were fully optimized via the conjugate gradient method until the ion forces on each atom were less than 10^{-8} eV·Å^{-1}.

3 Results and discussion

3.1 Microstructure of the EBCs before CMAS exposure

Figure 1 shows the microstructures of the as-sprayed porous YbMS and the dense aluminum-modified coatings. The total coating thickness is approximately 200 μm, comprising a top YbMS layer with a thickness of (95.3±10.2) μm, an intermediate mullite layer with a thickness of (50.3±8.3) μm, and a Si bond layer with a thickness of (50.4±11.1) μm, exhibiting a typical layered architecture. Some channel cracks and many intralayer and interlayer cracks were observed in the as-sprayed YbMS coating (Figs. 1(a) and 1(b)), similar to the previously reported YbDS coating (CTE: 4.5×10^{-6} K^{-1}) [25], which was caused primarily by high quenching stresses and insufficient substrate heating during deposition. Notably, the higher CTE of YbMS (7.4×10^{-6} K^{-1}) than that of the SiC substrate led to large tensile stresses during the cooling process, resulting in channel cracks

Table 1 Deposition parameters of the YbMS/mullite/Si EBCs by the APS

Materials	Power (kW)	Plasma gas (slpm)	Feed rate (g·min^{-1})	Stand-off distance (mm)	Preheating (°C)
YbMS	40	Ar/H_2 = 43:8	23	130	~200
Mullite	40	Ar/H_2 = 43:8	14	130	~200
Si	36	Ar/H_2 = 40:3	14	130	~200

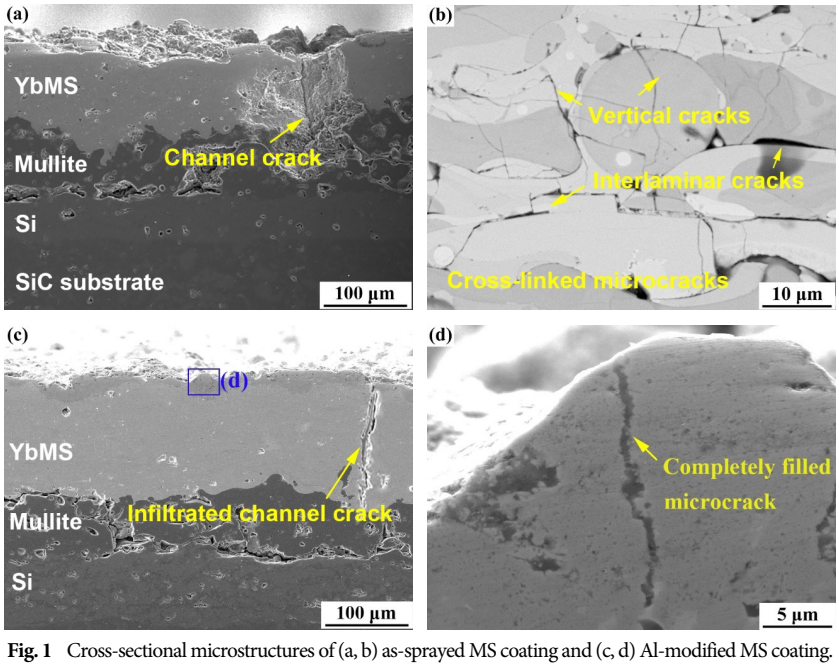

Fig. 1 Cross-sectional microstructures of (a, b) as-sprayed MS coating and (c, d) Al-modified MS coating.

(Figs. 1(a) and 1(b)). On the basis of five representative cross-sectional images per sample, the porosity of the sprayed top layer was estimated to be 6.8%±1.3%. These interconnected pores and microcracks—especially channel cracks—provide rapid pathways for environmental corrosion (such as CMAS), undoubtedly accelerating corrosion, oxidation, and premature coating failure. Consequently, eliminating sprayed porosity is crucial for enhancing the resistance of YbMS coatings to permeation corrosion.

After modification, aluminum deeply filled the microcracks, as indicated in Figs. 1(c) and 1(d), which is consistent with previous results [24–26]. Nanoscale converging cracks, regardless of orientation (vertical or lateral), can be infiltrated by capillary pressure. To achieve sufficient infiltration into large-scale, highly divergent pores, an assistant pressure of 100 kPa was applied. The measured porosity decreased to 1.3%±0.4%. The rapid penetration pathways for environmental corrosion were effectively blocked, thereby enhancing the long-term durability of YbMS coatings in CMAS environments.

Figure 2 shows backscattered electron (BSE)-mode images of the near-surface region for the as-sprayed and Al-modified coatings. Different contrasts correspond to distinct phase compositions, as shown in Table 2. In the as-sprayed coating (Fig. 2(a)), the dark areas correspond to the YbMS phase, whereas the bright regions represent Si-lean silicates and Yb_2O_3—formed by silica evaporation in the high-temperature plasma flame. After modification, a distinct darker contrast-modified layer with a uniform thickness of (16.1±2.6) μm was observed on the YbMS surface, as shown in Fig. 2(b). The primary phase of the surface-modified layer was identified as YbAG (Table 2), which is formed via the *in situ* reaction of aluminum with YbMS [24]. Notably, the quantitative analysis of light element (O) content via EDS is semiquantitative and may involve significant errors. The ratio of cations (Yb, Al, and Si) is considered more reliable. This newly formed layer acts as a physical barrier between the YbMS and CMAS melts, preventing them from reacting directly.

3.2 Phase evolution during CMAS exposure

DSC analysis was performed on pure CMAS powder, CMAS/YbMS, and CMAS/YbAG mixtures from room temperature to 1400 °C (Fig. 3). An endothermic peak at approximately 1205 °C is observed in all three systems, corresponding to the initial melting temperature of CMAS [25], confirming that the addition of YbMS or YbAG did not delay the initial melting of CMAS. This is a critical trigger for the corrosive reaction. However, a sharp endothermic peak appears at approximately 1338 °C exclusively in the CMAS/YbMS curve, indicating that a corrosion reaction occurred between YbMS and CMAS. Conversely, no additional peaks appeared in the CMAS/YbAG mixture curve after melting, suggesting superior thermodynamic stability and the absence of significant reactions at high temperatures.

Figure 4 shows the surface phase compositions of the coatings during CMAS interactions at 1400 °C. The as-sprayed coating (Fig. 4(a)) consists primarily of the YbMS phase (PDF#40-0386), while the previously mentioned Yb_2O_3 was undetected, possibly because its concentration was below the detection limit. The CMAS powder, which was heated separately to 1400 °C (as shown in the black spectrogram), consists primarily of cordierite ($Mg_2Al_4Si_5O_{18}$, PDF#13-0294). After 5 h of exposure, the MS coating exhibited the appearance of the YbDS phase (PDF#25-1345) and the Mg–Al garnet phase ($Mg_3Al_2(SiO_4)_3$, PDF#89-1490), confirming a chemical reaction between YbMS and CMAS. Increasing the exposure time to 25 h promoted the formation of sapphirine ($(Al_5Mg_3)(Al_4Si_2)O_{20}$, PDF#44-1430). According to the $MgO–Al_2O_3–SiO_2$ ternary phase diagram, cordierite transforms into sapphirine with increasing Al_2O_3 and SiO_2 concentrations [27], suggesting that the mullite layer is severely corroded.

After aluminum modification, the surface is primarily composed of the YbAG phase ($Yb_3Al_5O_{12}$, PDF#23-1476), as shown in Fig. 4(b). In addition, the Yb_3Si_5 phase (PDF#33-1456) forms during processing due to oxygen deficiency and is subsequently oxidized quickly [26]. Upon CMAS exposure, the YbDS phase is formed and gradually increases over time, indicating YbAG degradation and a YbMS-to-YbDS phase transition. Notably, some YbDS arises from the oxidation of Yb_3Si_5. Additionally, the YbAG diffraction peaks shift to lower angles, which is likely due to the change in the lattice parameters caused by the elemental solid solutions. Unlike the sprayed MS coating, no sapphirine phase was detected, demonstrating that the Al-modified YbMS coating has higher CMAS stability.

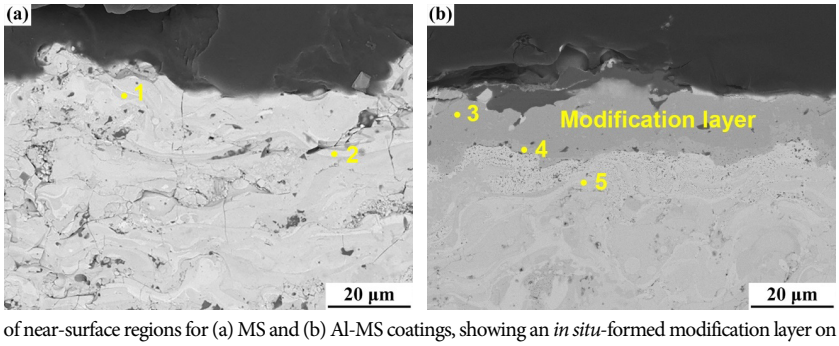

Fig. 2 BSE-mode images of near-surface regions for (a) MS and (b) Al-MS coatings, showing an *in situ*-formed modification layer on surface after modification.

Table 2 Elemental composition of the points in Fig. 2 measured via EDS

Sample	Point	Composition (at%)				Phase
		Yb	Si	O	Al	
MS	1	26	12	62	—	YbMS
	2	39	5	55	—	Yb_2O_3
Al-MS	3	13	—	66	21	YbAG
	4	22	—	42	36	YbAG
	5	26	10	64	—	YbMS

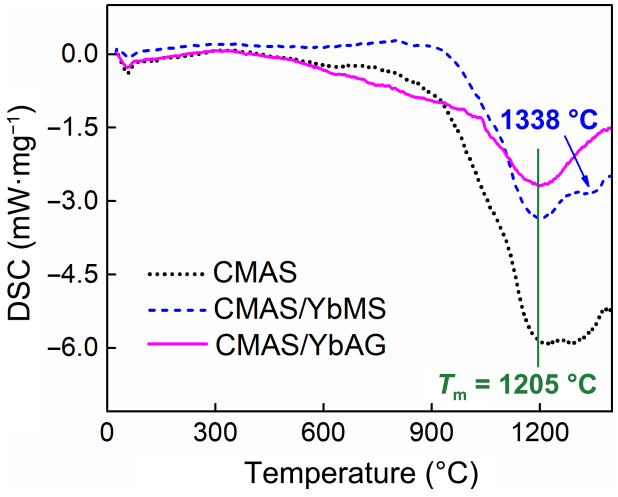

Fig. 3 DSC curves of CMAS powder, CMAS/YbMS, and CMAS/YbAG mixtures.

3.3 Microstructure evolution during CMAS exposure

3.3.1 *Evolution of the MS coating*

Figure 5 shows the cross-sectional microstructure of the YbMS coating after 5 h of exposure to the CMAS melt at 1400 °C. The melt attacked the surface, resulting in severe dissolution of the YbMS layer. The measured residual top coat thickness was (37.6±10.5) μm, and the recession thickness was (57.4±10.7) μm. Gradually dissolved phases reprecipitated in the residual melt, forming a "leaf"-like structure, accompanied by a discontinuous corrosion layer featuring numerous faceted crystals (Fig. 5(a)). The surface layer exhibited two distinct regions (Fig. 5(b)). The elemental compositions of each region are listed in Table 3. It can be inferred that the dissolved and outer-adhered darker facets (Points I and II) represent Mg-dissolved garnets, a phenomenon previously observed in the YbDS system, corresponding to silicate garnets [26]. In contrast, the inner lighter facets (Point III) consist

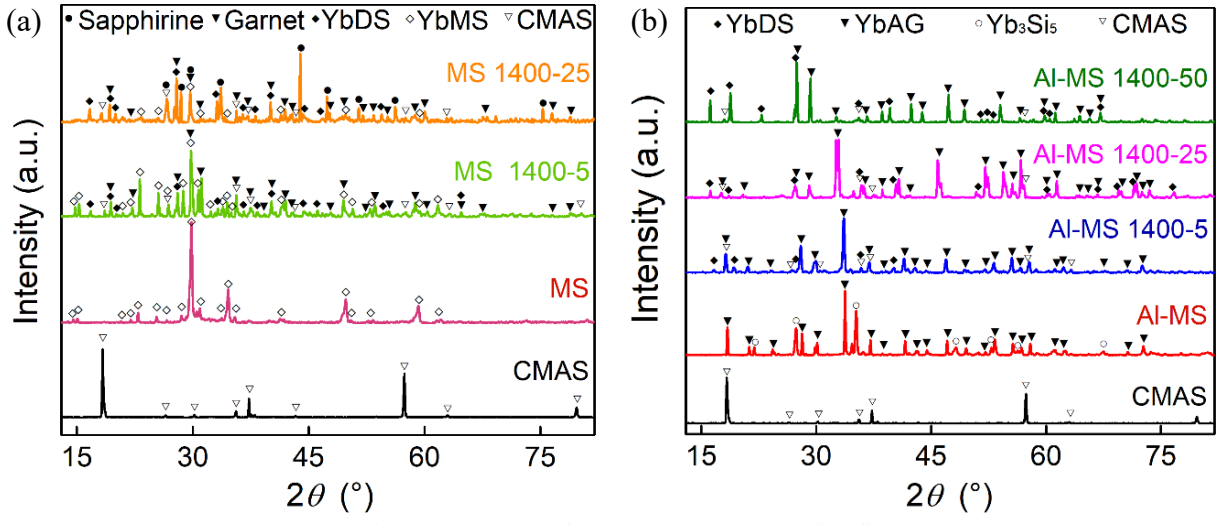

Fig. 4 Phase evolution of (a) MS and (b) Al-MS after CMAS corrosion at 1400 °C for different exposure periods.

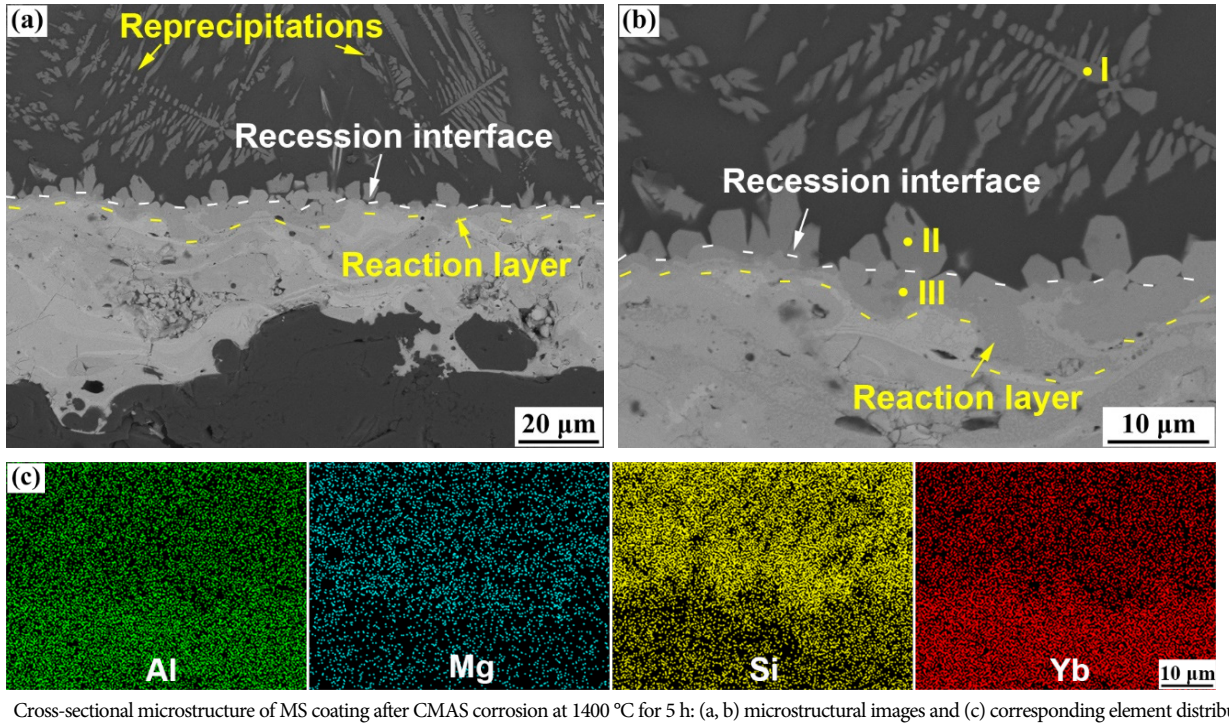

Fig. 5 Cross-sectional microstructure of MS coating after CMAS corrosion at 1400 °C for 5 h: (a, b) microstructural images and (c) corresponding element distribution mappings in (b).

of YbDS with trace amounts of Mg, indicating a preferential reaction between YbMS and CMAS-derived silica. The elemental mappings in Fig. 5(c) reveals that the corrosion layer plays a certain role in blocking melt penetration, but YbMS is highly reactive with CMAS, demonstrating that its overall corrosion resistance is inadequate.

TEM characterization was conducted to identify the phases observed via SEM and EDS at the YbMS/CMAS recession interface. A HADDF-scanning transmission electron microscopy (STEM) image (Fig. 6(a)) of a FIB-milled slice from the interface reveals adhered garnet facets (Region A), a YbDS reaction layer (Region B), and the original YbMS matrix. Figure 6(b) shows corresponding elemental maps, highlighting the elevated Al and Mg concentrations in the reaction layer. HRTEM images of regions A and B marked in Figs. 6(a) and 6(c) and the corresponding SEAD patterns (Figs. 6(e) and 6(f)) confirm that phase A is Al–Mg garnet ($Mg_3Al_2(SiO_4)_3$, PDF#89-1490) and that phase B is YbDS (PDF#25-1345). HRTEM and SEAD analyses of Figs. 6(d) and 6(g) demonstrate that the residual CMAS (region C) has an amorphous structure with significantly reduced Mg and Al contents. This indicates that YbMS readily reacts with CMAS to form YbDS, subsequently forming a garnet solid solution.

After 25 h of prolonged exposure, the cross-sectional microstructures of the YbMS coating (Fig. 7) revealed that the entire coating, including the YbMS top layer and underlying mullite layer, was completely dissolved in the CMAS melt, with a total recession thickness of approximately 145 μm. As previously reported, numerous bubbles emerged on the surface after 25 h of exposure, whereas the phenomenon was not pronounced at the early 5 h stage [25]. This discrepancy is attributed to the continuous corrosion reaction reducing the melt viscosity, thereby facilitating the escape of gaseous reaction products [18]. The

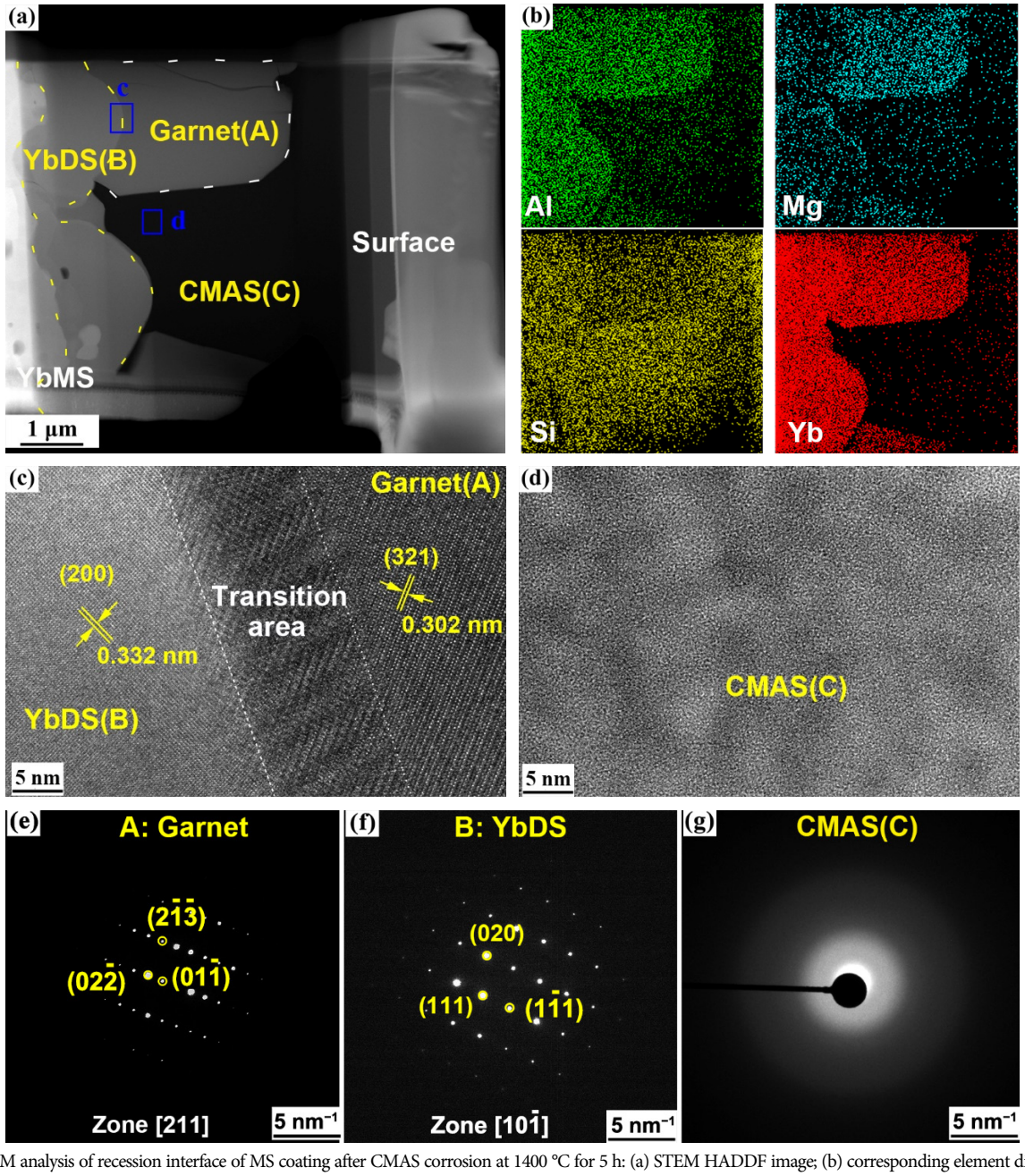

Fig. 6 TEM analysis of recession interface of MS coating after CMAS corrosion at 1400 °C for 5 h: (a) STEM HADDF image; (b) corresponding element distribution; (c, d) HRTEM images of Regions A and B marked in (a); (e–g) SEAD analysis and each phase.

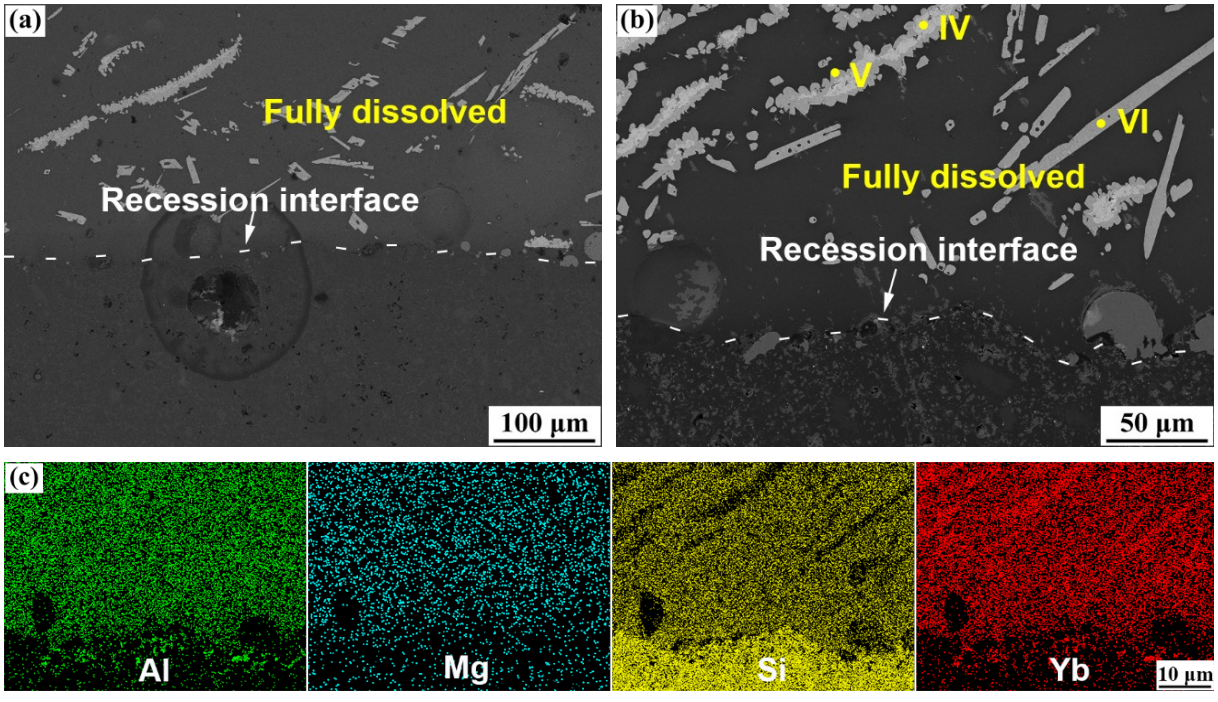

Fig. 7 Cross-sectional microstructure of MS coating after CMAS corrosion at 1400 °C for 25 h: (a, b) microstructural images and (c) corresponding element distribution maps in (b).

reprecipitates in the residual melt exhibit a core–shell structure: The shell comprises the YbDS phase, while the core retains the YbMS phase (Fig. 7(b) and Table 3). Notably, no garnet phase or dissolved Al/Mg elements were detected, which is primarily due to the low Al and Mg contents in the residual melt. For the previous YbDS coating, a thin YbDS layer remained after 25 h of exposure at 1400 °C. This phenomenon indicates that the CMAS melt has preferential reactivity with YbMS, leading to a faster dissolution rate of YbMS than of YbDS. The absence of the mullite phase in the residual melt indicates a concurrent reaction between mullite and CMAS. These results collectively confirm that YbMS degrades rapidly at 1400 °C, demonstrating its extreme susceptibility to corrosion by CMAS melt.

Garnet existed as the primary phase after 4 h of corrosion but disappeared after 25 h, indicating that the reaction pathway was dynamic. The initial stage was governed by kinetic factors, with high local cation concentrations (such as Al^{3+}, Mg^{2+}, and Yb^{3+}) driving the rapid formation of garnets. As the exposure time increased, the system gradually reached thermodynamic equilibrium. The consumption of Yb and Al at the coating interface promoted the dissolution of garnet and the precipitation of more stable phases (such as sapphirine) [27]. This evolution underscores the importance of evaluating the CMAS resistance of coatings over extended durations to assess their long-term phase stability.

3.3.2 *Evolution of the aluminum-modified MS coating*

Figure 8 shows the cross-sectional microstructure of the Al-modified YbMS coating after 5 h of exposure to the CMAS melt at 1400 °C. Although dissolution occurred at the melt/coating interface, the modified YbAG layer remained intact and tightly adhered to the YbMS matrix, as shown in Fig. 8(a). No pores or cracks formed within the coating. The measured top coat thickness was (93.2±9.0) μm, comparable to the as-sprayed state, with a recession thickness of only (2.4±1.1) μm—this can be seen from the isolated small facets dissolved into the melt or adhered to the surface (Fig. 8(b)). This corresponds to a thickness reduction

Table 3 Point elemental compositions of MS coatings in Figs. 5 and 7 measured via EDS

Exposure time (h)	Point	Composition (at%)					Phase
		Yb	Si	Al	Mg	Ca	
5	I	27	35	15	20	3	Garnet ss
	II	31	30	16	23	—	Garnet ss
	III	48	40	3	9	—	YbDS
25	IV	64	36	—	—	—	YbMS
	V	47	53	—	—	—	YbDS
	VI	45	55	—	—	—	YbDS

of over 95%, which is significantly lower than the thickness of the unmodified YbMS coating.

Elemental analysis revealed that the dissolved phase (Point I') was a YbAG garnet solid solution containing Mg and Si substitutions (YbAG ss) (Table 4), whereas the inner phase (Point II') consisted of pure YbAG without solid solutions. The elemental distribution mappings in Fig. 8(c) confirm that the YbAG layer acted as a diffusion barrier, hindering the penetration of CMAS-derived Mg. Additionally, the dense structure of the coating also suppressed rapid melt permeation. However, silica diffusion persisted, reacting with the underlying YbMS to form YbDS (Point III'), a phenomenon analogous to that observed in unmodified YbMS coatings. Overall, the uniform YbAG layer and dense structure effectively prevent inward CMAS diffusion, significantly improving the corrosion resistance of the YbMS coatings.

Figure 9 presents TEM images of a foil extracted from the recession interface of the Al-modified YbMS coating. The HADDF image in Fig. 9(a) reveals coarsened large grains and nanopores near the coating surface. HRTEM and SEAD analyses (Fig. 9(b)) confirm that these coarse grains are the YbAG garnet phase (PDF#23-1476). The amorphous CMAS melt infiltrates through the YbAG grains to a limited depth and forms the YbDS phase at the grain boundaries (Fig. 9(c)), which is consistent with the SEM and XRD findings. Figure 9(d) further shows the

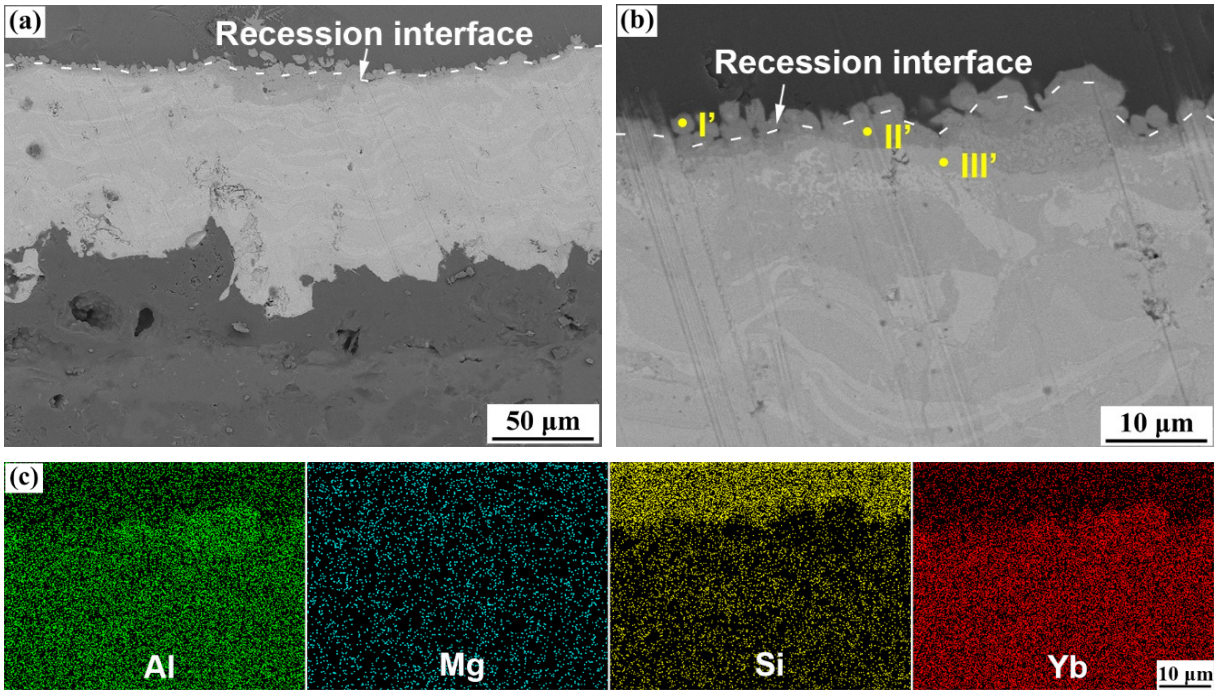

Fig. 8 Cross-sectional microstructure-modified Al-MS coating at 1400 °C for 5 h: (a, b) microstructural images and (c) corresponding element distribution maps in (b).

Table 4 Point elemental compositions of modified Al-MS coatings in Figs. 8–11 measured via EDS

Exposure time (h)	Point	Composition (at%)					Phase
		Yb	Si	Al	Mg	Ca	
5	I'	24	34	21	18	3	YbAG ss
	II'	37	2	61	—	—	YbAG
	III'	45	55	—	—	—	YbDS
25	IV'	24	35	20	18	3	YbAG ss
	V'	34	12	43	11	—	YbAG ss
	VI'	36	—	64	—	—	YbAG
	VII'	44	56	—	—	—	YbDS
50	VIII'	33	7	54	6	—	YbAG
	IX'	46	54	—	—	—	YbDS

presence of numerous fine YbAG grains within the modified layer, demonstrating that the modification process created microstructural heterogeneity.

After 25 h of exposure to CMAS melt at 1400 °C, cross-sectional images of the Al-modified YbMS coating are shown in Fig. 10. The dissolution at the melt/coating interface increased noticeably; however, the measured residual top coat thickness remained at (91.3±10.5) μm, with the recession thickness slightly increasing to (4.8±2.0) μm, as shown in Fig. 10(a). This indicates a slow dissolution rate of YbAG. Additionally, the dissolution inside the melt and at the melt/YbAG interface became coarser, suggesting a reduced rate of new solid solution formation [28]. The composition of the dissolved phases (Points IV' and V') in Fig. 10(b) was confirmed to be YbAG solid solutions, as shown in Table 4. The underlying dense layer (Point VI') consisted of initially formed YbAG without solid solution elements, whereas the newly formed YbDS layer (Point VII') was generated by the reaction of YbMS and CMAS, which is consistent with the XRD results in Fig. 4. The modified layer effectively prevented the infiltration of corrosive elements into the YbMS coating, as illustrated in Fig. 10(c). These findings indicate that melt penetration and coating recession are significantly reduced after extended exposure, further confirming the exceptional CMAS corrosion resistance of the aluminum-modified YbMS coating.

The microstructural evolution of the Al-modified YbMS coating after 50 h of exposure is shown in Fig. 11. A thin residual glass layer covered the surface of the sample, and the coating surface became rough with numerous coarse facets (Fig. 11(a)). The previously observed dissolved phase was completely removed by the melt. The residual thickness of the coating was measured to be (88.6±7.5) μm. The recession thickness was limited to (6.4±2.6) μm, demonstrating a very low recession rate. Although more than 50% of the initially formed YbAG modification layer (Point VIII') had been consumed, it remained dense and tightly adhered to the MS coating (Fig. 11(b)). This indicates that the corrosion reaction reached equilibrium as CMAS was gradually consumed. Furthermore, the YbDS reaction layer (Point IX') thickened to approximately 10 μm, which is consistent with the XRD results in Fig. 4(b). These results confirm that the YbAG surface modification layer effectively protects the YbMS coating from recession, thus ensuring its long-term resistance to CMAS corrosion.

3.4 Recession rates during CMAS exposure

Figure 12 shows the recession rates of the coatings during CMAS exposure at different temperatures, with the recession depth normalized as the ratio of recession thickness to as-sprayed coating thickness. After 5 h of exposure, the average recession

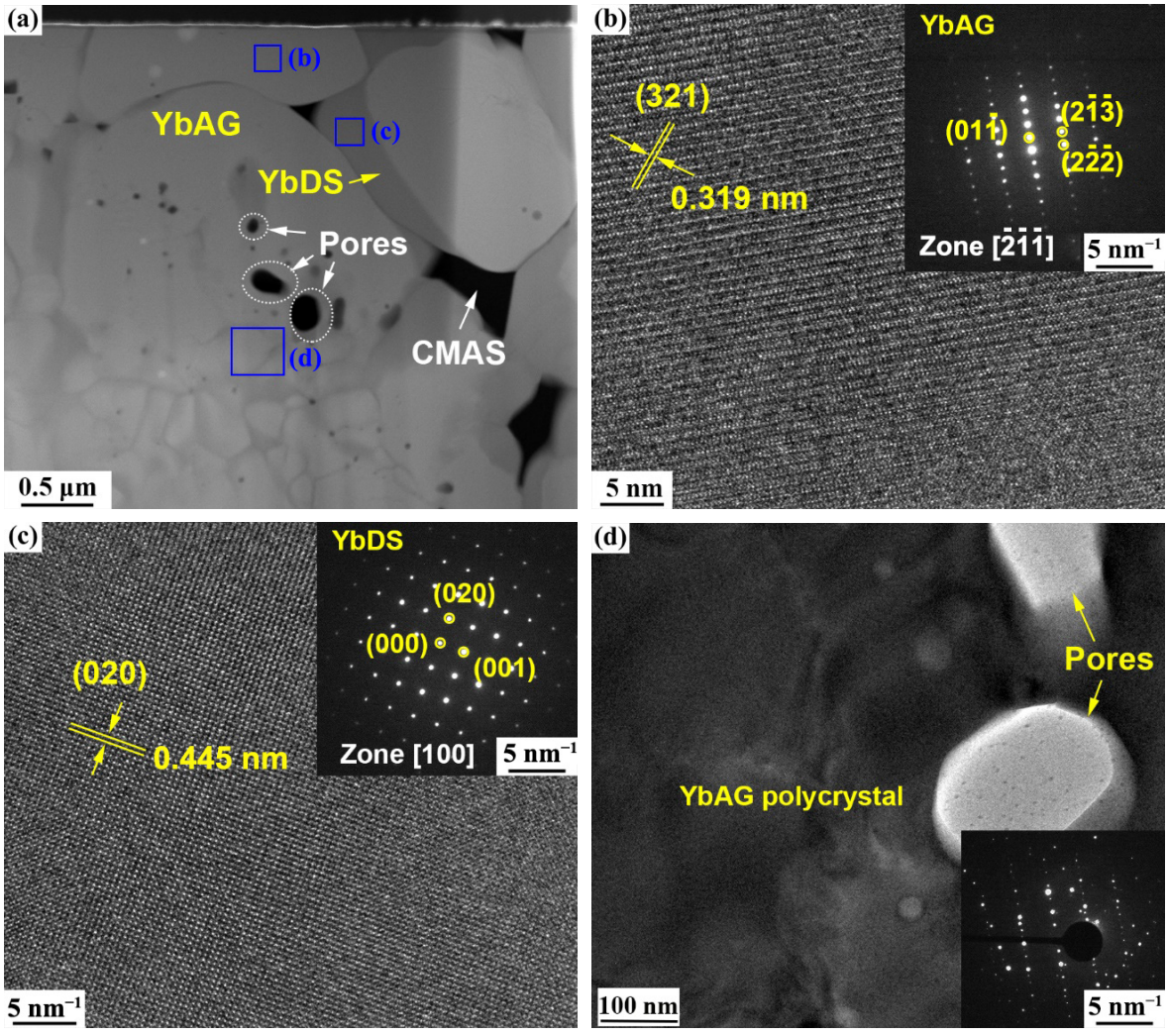

Fig. 9 TEM analysis of recession interface of modified Al-MS coating after CMAS corrosion at 1400 °C for 5 h: (a) STEM HADDF image; (b–d) HRTEM images and corresponding SEAD analyses of selected regions marked in (a).

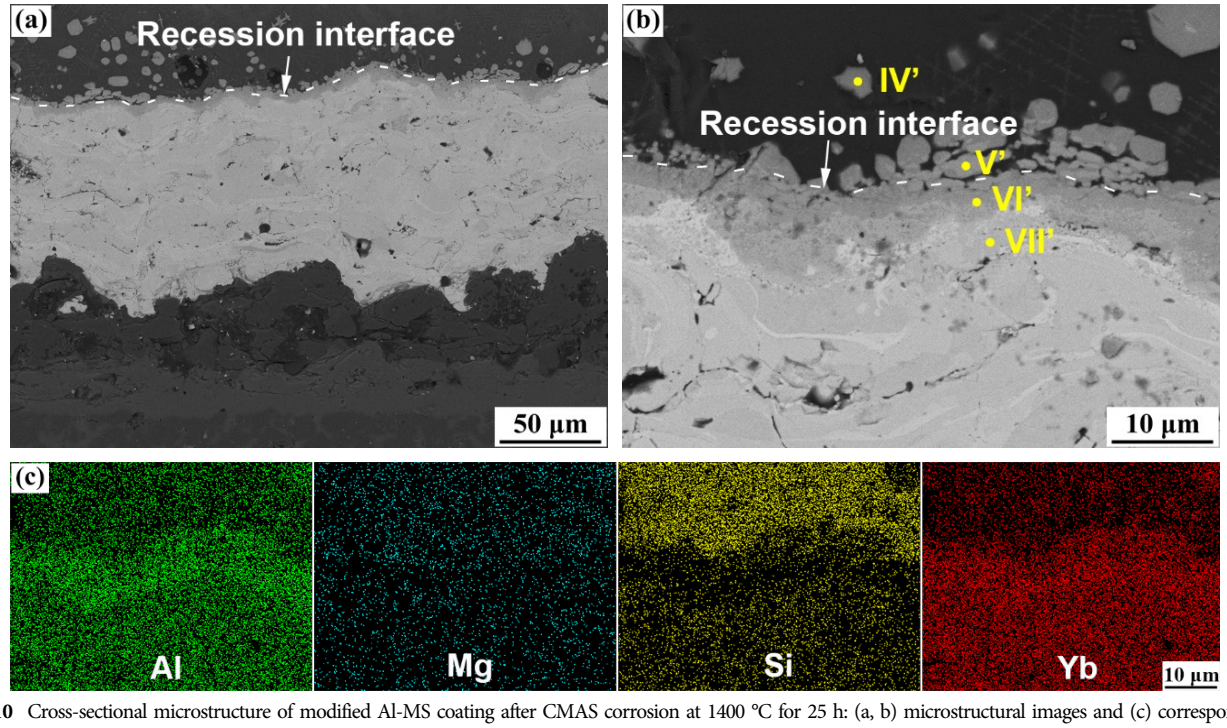

Fig. 10 Cross-sectional microstructure of modified Al-MS coating after CMAS corrosion at 1400 °C for 25 h: (a, b) microstructural images and (c) corresponding element distribution maps in (b).

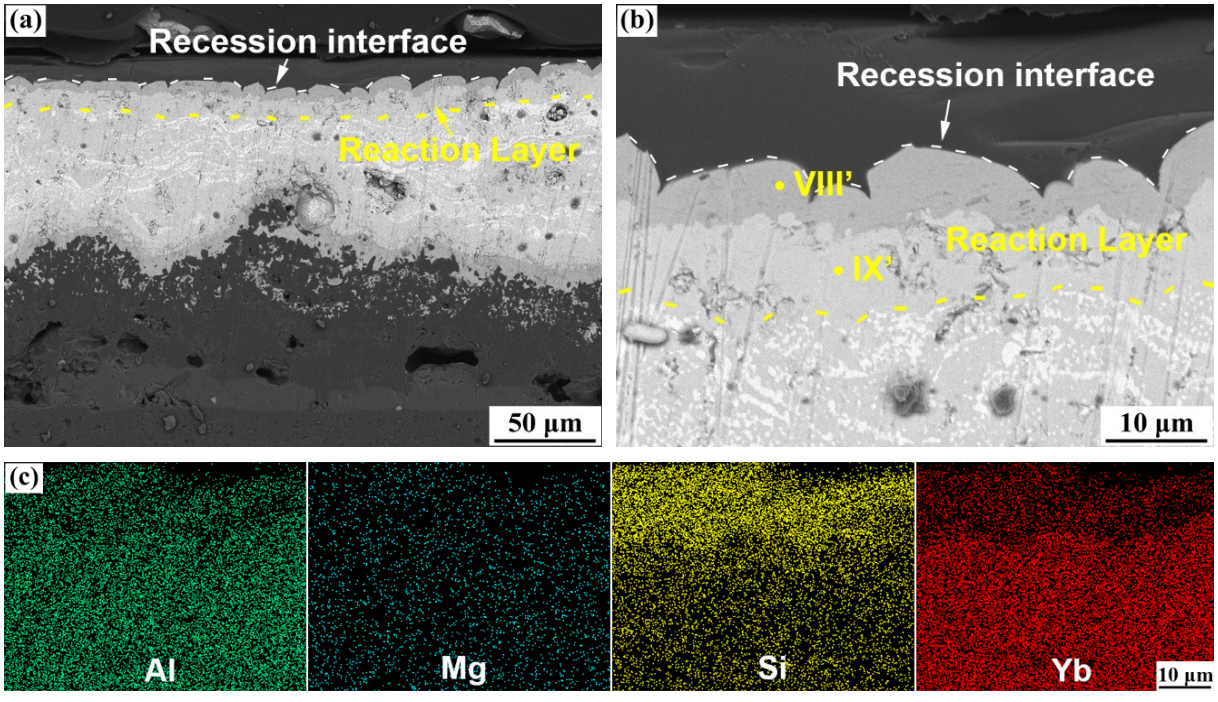

Fig. 11 Cross-sectional microstructure of modified Al-MS coating after CMAS corrosion at 1400 °C for 50 h: (a, b) microstructural images and (c) corresponding element distribution maps in (b).

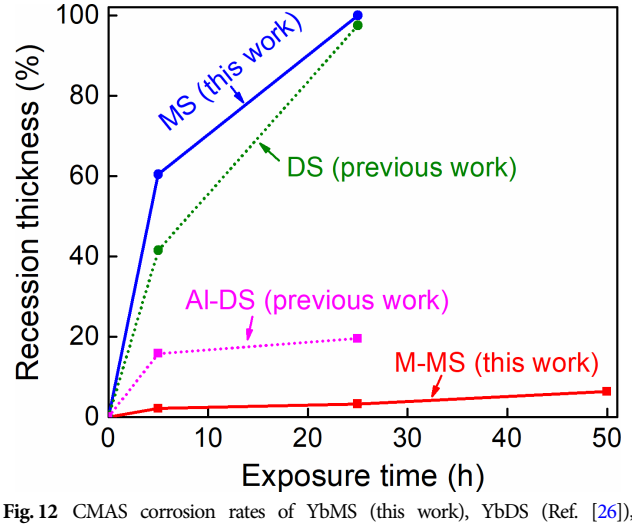

Fig. 12 CMAS corrosion rates of YbMS (this work), YbDS (Ref. [26]), aluminum-modified Al-YbMS (this work), and Al-YbDS (Ref. [26]) coatings at 1400 °C.

thickness of the YbMS coating was approximately 63% (Fig. 5), whereas the recession thickness of the modified Al-MS coating was only 2% (Fig. 8). After exposure for 25 h, the YbMS coating completely dissolved (Fig. 7), and the underlying mullite and Si layers also disappeared. To maintain consistency with previous YbDS system studies, only the top layer recession was quantified. At this stage, the recession depth of the YbMS coating reached 100%, while the recession thickness of the modified Al-MS coating was 3%. Even after 50 h, with a slight increase in recession depth to 6% (Fig. 12), the YbAG layer remained intact and tightly adhered, demonstrating a significantly reduced CMAS corrosion rate for the Al-MS coating and a corrosion life that was extended by at least 10 times.

The recession data for the previous DS and modified Al-DS systems are included in Fig. 12 for comparison. To enable a direct and fair comparison of all the coating systems (MS, DS, Al-MS, and Al-DS), the recession thickness was further normalized to the original thickness of the entire coating. This dimensionless approach eliminates the influence of initial thickness variations and accurately reflects the corrosion resistance of the material. In the first 4 h, the corrosion rate of the YbDS coating was lower than that of the YbMS coating; after 25 h, only a thin YbDS film remained, and the Si layer remained intact, confirming its lower average corrosion rate and superior corrosion resistance. Notably, under the same conditions, the YbAG layer in the previously modified Al-DS coating gradually dissolved within 25 h and then rapidly peeled off, indicating a faster corrosion rate than that of the Al-MS coating. These results confirm that Al modification is an effective strategy for mitigating CMAS-induced degradation of ytterbium silicate coatings.

3.5 Mechanism of aluminum modification in MS and DS coatings

3.5.1 *Microstructural differences in surface modification layers*

The corrosion reaction results reveal that both the Al-modified YbMS (in this study) and the Al-modified YbDS (in a previous study [26]) systems follow similar protective mechanisms, which are achieved primarily through the *in situ* formation of a YbAG layer. However, significant differences exist in their performance: The Al-YbMS coating results in a significantly lower corrosion rate and superior longevity (Fig. 12). Despite similar reaction products, the significant disparity in performance suggests a fundamental difference in the precise nature of the protective layer. These differences are likely attributable to the microstructural differences resulting from the distinct crystal structures of the YbMS and YbDS coatings.

To clarify the fundamental reasons for this performance enhancement and investigate the atomistic-level mechanism, a detailed TEM nanoscale characterization was conducted to compare the crystal structures and interfacial reaction products formed in each system, as shown in Fig. 13. Notably, the YbAG

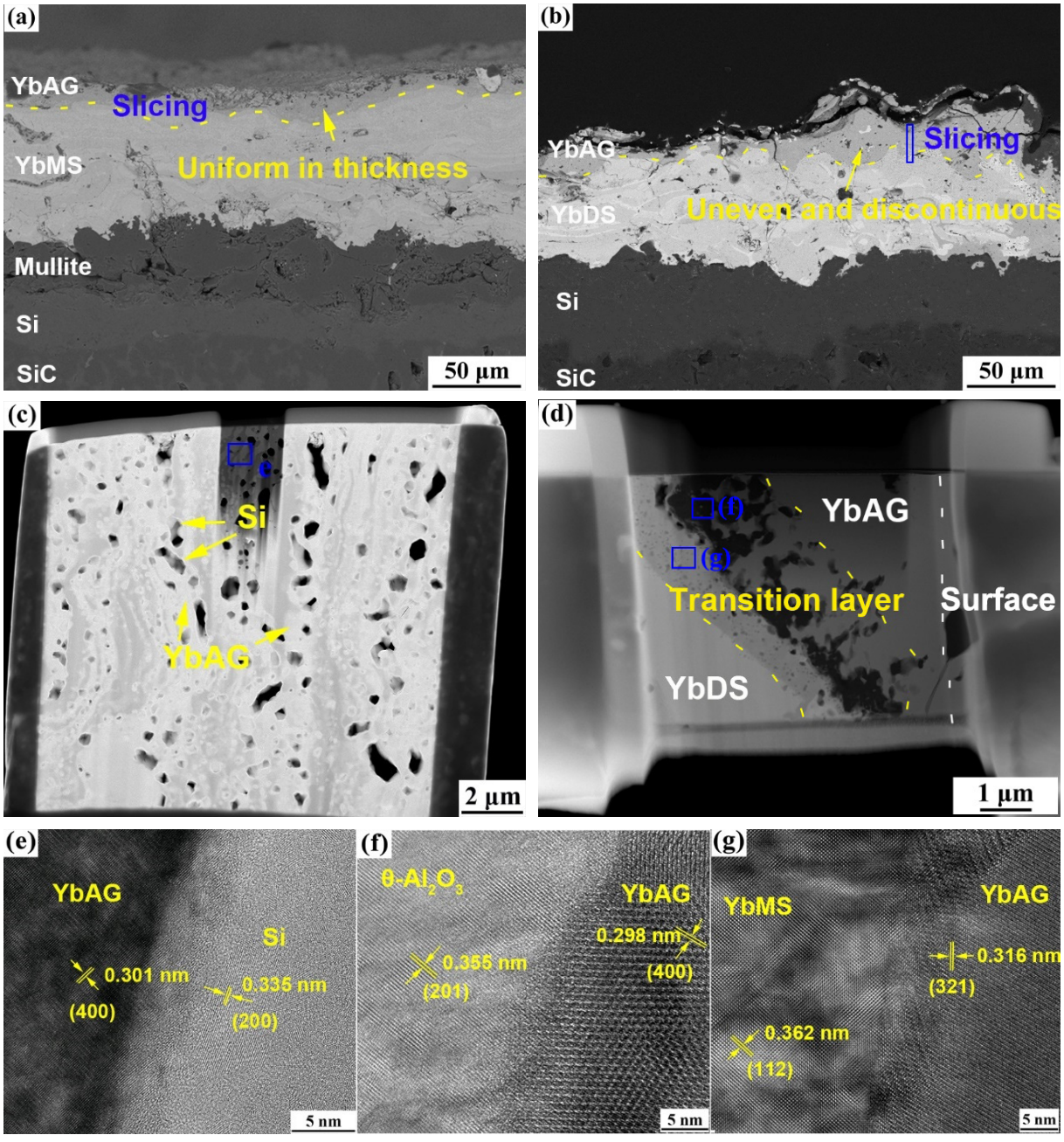

Fig. 13 Microstructure of modified layers of (a, c, e) Al-MS and (b, d, f) Al-DS coatings: (a, b) BSE-SEM cross-sectional images of two coatings; (c, d) TEM HADDF images of two coatings; (e–g) HRTEM images of selected areas in (c) and (d).

layer in the Al–MS coating has a uniform thickness along the surface (Fig. 13(a)), whereas the thickness of the Al-DS coating varies considerably, ranging from 1–2 μm to tens of micrometers (Fig. 13(b)). Slices of the two surfaces in Figs. 13(c) and 13(d) further validate this discrepancy. HRTEM analysis of the Al-MS surface revealed a continuous YbAG matrix with homogeneously dispersed Si (PDF#72-1088), as shown in Fig. 13(e). In contrast, the Al-DS coating formed a thicker transition layer comprising two distinct regions. The HRTEM results identify the outer dark "clusters" as θ-Al_2O_3 (PDF#86-1410), whereas the inner lighter layer is primarily composed of the YbMS phase (PDF#40-0386), as is evident in Figs. 13(f) and 13(g). This indicates an incomplete *in situ* reaction, as the coexistence of YbMS and Al_2O_3 phases suggests insufficient thermodynamic equilibrium. Notably, the CMAS corrosion resistances of YbMS and Al_2O_3 are significantly weaker than that of YbAG [26,29]. Consequently, the extremely thin YbAG zone and the incompletely reacted region in the Al-DS modification layer collectively limit its overall resistance to CMAS degradation.

3.5.2 *Atomic-scale reactions during aluminum modification*

The crystal structures of YbMS, YbDS, and YbAG are shown in Fig. 14. YbMS in Fig. 14(a) shows monoclinic symmetry with *I*2/*a* space groups (cell parameters a = 10.29 Å, b = 12.38 Å, c = 6.68 Å, and β = 102.5°) [2,30]. Each Si in the silicates is surrounded by four oxygen atoms, forming tetrahedral $[SiO_4]^{4-}$ units. The YbMS lattice contains only isolated $[SiO_4]^{4-}$ tetrahedrons, each connected to Yb^{3+} ions through Si–O–Yb bonds (labeled Si–O_b, marked with red circles in the figure). In contrast, the YbDS lattice features a corner-sharing double tetrahedron group $[Si_2O_7]^{6-}$, with edges linked to Yb^{3+} ions, which results in a very low degree of distortion [12]. Figure 14(c) shows the cubic lattice (space group of *Ia*3*d*) of

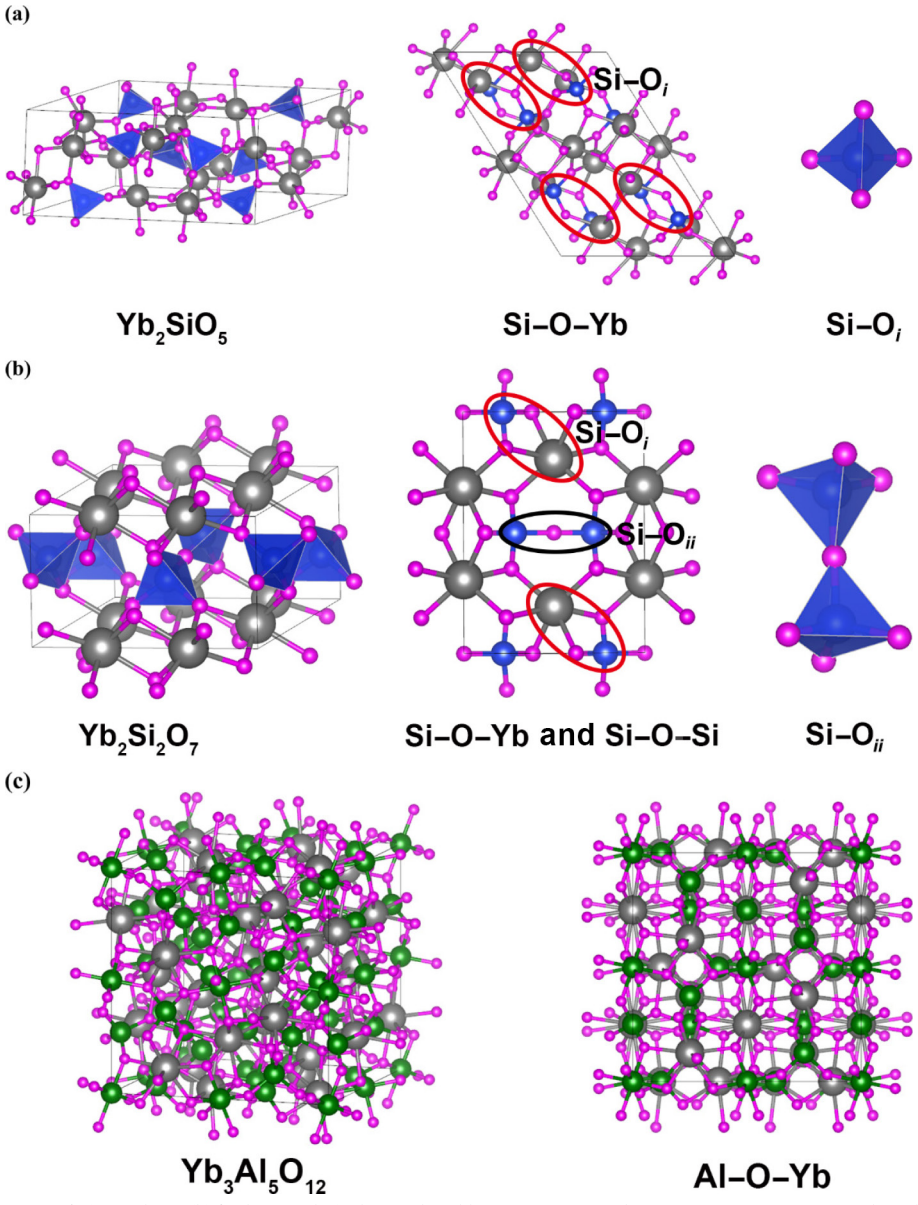

Fig. 14 Crystal structures of (a) X2-YbMS, (b) β-YbDS, and (c) YbAG, where blue atoms are Si, pink atoms are O, gray atoms are Yb, and green atoms are Al.

YbAG garnet, where Al and O atoms form two types of units: [AlO_4] tetrahedra and [AlO_6] octahedra [31]. Therefore, YbDS contains two different types of Si–O bonds: the aforementioned Si–O_i bond and the Si–O–Si bond in the structure (labeled Si–O_{ii} and marked with a black circle in the figure).

The mean Si–O distance for both the isolate $[SiO_4]^{4-}$ and the double $[Si_2O_7]^{6-}$ tetrahedron is 1.63 Å. However, the different polarities of the linked Yb and Si atoms lead to variations in Si–O bond energies, which were calculated to be 123.5 kJ·mol^{-1} for Si–O_i and 146.7 kJ·mol^{-1} for Si–O_{ii} bonds in the YbDS lattice and 127.4 kJ·mol^{-1} for Si–O_i in the YbMS lattice, as shown in Fig. 15. Notably, the difference in Si–O_i bond energies between the two lattices arises from the longer Yb–O length in YbMS (2.33 Å) than in YbDS (2.24 Å). The calculated bond energy of Al–O in the Al_2O_3 lattice is 171.7 kJ·mol^{-1}, which is lower than that of the Yb–O bonds in silicates (264–266 kJ·mol^{-1}), indicating a lower tendency for Al to interact with Yb–O bonds. Although the energy of the Al–O bond is significantly greater than that of the Si–O_i bond, the difference is not significant compared with that of the Si–O_{ii} bond, indicating a preferred interaction of Al with Si–O bonds, especially the Si–O_i bond.

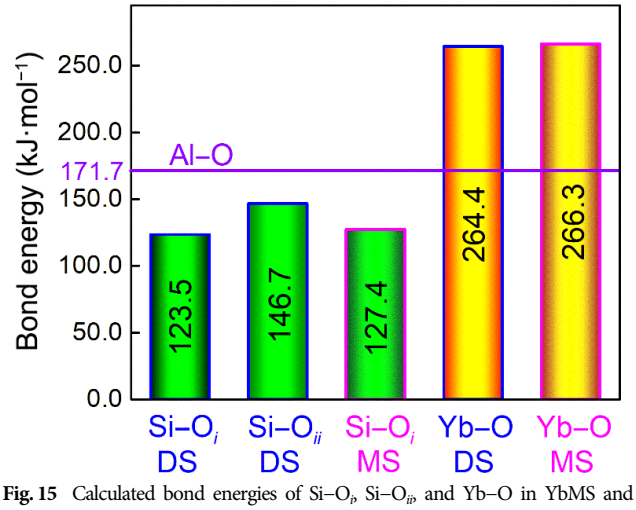

Fig. 15 Calculated bond energies of Si–O_i, Si–O_{ii}, and Yb–O in YbMS and YbDS lattices, along with Al–O in the Al_2O_3 lattice.

It has been reported that the standard reduction potential of Al^{3+}→Al is −1.66 V, whereas that of Yb^{3+}→Yb is −2.37 V, the latter

being more negative [32]. These findings demonstrate that the reducing power of Al is insufficient to directly reduce Yb^{3+}.

Accordingly, it can be inferred that the most likely *in situ* reactions in the YbMS system are as Reactions (1) and (2):

$$4Al + 3Yb_2SiO_5 \rightarrow 2Al_2O_3 + 3Yb_2O_3 + 3Si \quad (1)$$

$$5Al_2O_3 + 3Yb_2O_3 \rightarrow 2Yb_3Al_5O_{12} \quad (2)$$

In the YbDS system, Reaction (3) may also occur:

$$4Al + 3Yb_2Si_2O_7 \rightarrow 3Yb_2SiO_5 + 2Al_2O_3 + 3Si \quad (3)$$

The activation energies of the formation of YbAG from YbMS and YbDS are calculated to be 6.13 and 8.24 eV, respectively, indicating a higher energy barrier for the reaction from YbDS. This phenomenon can be attributed primarily to the abundant $Si–O_{ii}$ bonds in the YbDS lattice, which significantly increase the activation energy threshold of the reaction. The observation of Si, YbMS, and Al_2O_3 phases in the modified layers of both systems (Fig. 13) also validates the proposed reactions. Additionally, the presence of di-pyramidal groups in YbDS leads to a more complex network structure. This increased structural complexity is likely responsible for its superior stability during modification compared with YbMS.

The above reaction mechanisms can also be explained on the basis of the Yb_2O_3–SiO_2–Al_2O_3 ternary phase diagram [26], as shown in Fig. 16. When Al_2O_3 reacts with YbMS and YbDS in equilibrium (essentially a chemical reaction between the three oxides), the phase composition of the system evolves along the two red lines marked in Fig. 16. However, when metallic Al is used as a reactant, it first undergoes redox reactions with YbMS and YbDS, i.e., Reactions (1) and (3), resulting in the system composition being derived from the red equilibrium reaction lines. These redox reactions increase the contents of Yb_2O_3 and Al_2O_3 in the system, thus shifting the phase compositions downward to the left in the diagram. According to the actual phase composition, the products of the YbMS system are located primarily in the red shaded region and are predominantly composed of the YbAG phase. In contrast, the YbDS system first generates YbMS, which undoubtedly causes the reaction to deviate further from the equilibrium state. An enrichment of incompletely reacted YbMS and Al_2O_3 phases appears in the transition layer. Consequently, the complexity of the *in situ* reaction in the YbDS system limits the distribution uniformity of the thickness and phase of the modification layer, further compromising the stability of the modified layer when in contact with CMAS.

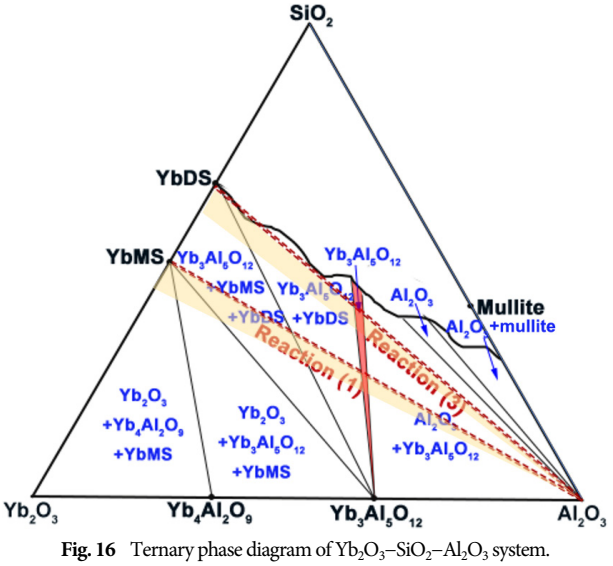

Fig. 16 Ternary phase diagram of Yb_2O_3–SiO_2–Al_2O_3 system.

The absorption behavior of aluminum on the YbMS and YbDS surfaces is another critical factor accounting for their divergent modification behaviors. The absorption energies of the aluminum atoms on the (100) crystal faces of YbMS and YbDS—with the lowest energy and therefore the predominant orientation during crystal growth—were calculated.

Three independent systems were fully geometrically optimized: (1) energy of the pure YbMS model ($E_{s–m}$) and the pure YbDS model ($E_{s–d}$); (2) energy of the isolated three-atom aluminum model (E_{Al}); and (3) energy of the Al-bounded YbMS mode ($E_{t–m}$) and the the Al-bounded YbDS model ($E_{t–d}$).

The absorption energy (E_{ads}) is determined as $E_{ads} = E_t - E_s - E_{Al}$. The calculated values for $E_{s–m}$, $E_{s–d}$, E_{Al}, $E_{t–m}$, and $E_{t–d}$ were 7.13, 5.49, 1.66, 7.37, and 5.86 eV, respectively. Accordingly, the absorption energies of aluminum on the YbMS and YbDS surfaces were determined to be −1.42 and −1.29 eV, respectively.

A negative absorption energy indicates that the adsorption process is exothermic and thermodynamically favorable. The more negative the absorption value is, the stronger the adsorption. The adsorption energy of YbMS is significantly lower than that of aluminum, suggesting that YbMS has a stronger affinity for aluminum, which facilitates subsequent chemical reactions during modification.

3.6 Corrosion resistance mechanism of aluminum-modified coatings

3.6.1 *CMAS-induced corrosion reactions*

Notably, significant corrosion occurred between YbMS and CMAS despite the melt's low Ca^{2+} content. The reaction products were identified as YbDS, garnet and its solid solutions via XRD, EDS, and TEM (Figs. 5–7). It can be inferred that partial YbMS first reacts to form YbDS, followed by silicate garnet formation—which is consistent with previous studies. MgO- and Al_2O_3-rich melts favor garnet over apatite formation in RE silicate systems, particularly in systems with smaller RE^{3+} ions such as Yb^{3+} [1,12]. The Yb_2O_3 phase in the top layer reacts with alumina to form $Yb_3Al_5O_{12}$ garnet [33–35], which can be described by the following chemical reactions between the MS coating and CMAS melt (Reactions (4)–(6)):

$$2.5Yb_2SiO_5 + 3MgO \cdot 3.5Al_2O_3 \cdot 2.5SiO_2(melt) \rightarrow Mg_3Al_2(SiO_4)_3 + Yb_3Al_2(AlO_4)_3 + Yb_2Si_2O_7 \quad (4)$$

$$3Yb_2O_3 + 5Al_2O_3(melt) \rightarrow 2Yb_3Al_2(AlO_4)_3 \quad (5)$$

$$Yb_2SiO_5 + SiO_2(melt) \rightarrow Yb_2Si_2O_7 \quad (6)$$

Initially, cation dissolution and reactions occur at the interface, mainly through atomic interactions. The cations in the coating (Yb^{3+} and Si^{4+}) dissolve into the melt, whereas the cations in CMAS (Al^{3+}, Mg^{2+}, and trace amounts of Ca^{2+}) diffuse into the coating. This interdiffusion creates a locally supersaturated region at the interface, where the chemical potential favors the nucleation of the silicate garnet phase, alumina garnet, and their solid solutions in the YbMS system. As the corrosion time increases and the concentration of reactive cations (Al^{3+}) decreases, Reactions (4) and (5) gradually reach equilibrium. The residual

melt maintains a high SiO_2 concentration, sustaining its corrosive potency. YbMS dissolution and Reaction (6) became dominant, as shown in Fig. 7. This confirms that RE DS exhibit superior CMAS resistance stability compared with their MS counterparts [36]. Thermodynamically, YbMS demonstrates high reactivity with CMAS, hindering the formation of a dense refractory product layer. This inherent limitation leads to its continuous and rapid corrosion when exposed to CMAS melt at elevated temperatures, as the lack of a protective layer allows the melt to penetrate unimpeded and undergo phase decomposition.

The corrosion mechanism of YbAG garnet with CMAS has been described in detail in our prior studies. The preconstructed YbAG layer prevents the interaction between YbMS and CMAS. Active Mg^{2+} cations substitute for Yb^{3+} in the lattice, whereas Si^{4+} replaces Al^{3+} to maintain charge balance, thereby forming a garnet solid solution. Garnet crystal structures have a solubility limit for corrosive elements such as Ca^{2+}, Mg^{2+}, and Si^{4+}. The solubility limit of Ca^{2+} in YAG is approximately 0.065%±0.015% at 1700 °C [37]. At 1400 °C, the solubility of Ca^{2+} in the YAG system is reported to be 11 at%, which is far below the theoretical maximum value of 37.5 at% [38]. Notably, the elemental composition of the reaction products detected in this study varied widely. One product in the YbMS system was identified as $(Yb_{2.48}Mg_{0.52})(Al_{0.68}Mg_{1.32})(Si_{2.4}Al_{0.6})O_{12}$ on the basis of the composition at point II in Table 3. Additionally, as determined from points V' and VIII' in Table 4, the products in the Al-MS system were $(Yb_{2.72}Mg_{0.28})(Al_{1.4}Mg_{0.6})(Al_{2.04}Si_{0.96})O_{12}$ and $(Yb_{2.64}Mg_{0.36})(Al_{1.88}Mg_{0.12})(Al_{2.44}Si_{0.56})O_{12}$, respectively. These components all exhibit charge imbalance, primarily due to significant measurement deviations (5%–10%) in the EDS method [8]. Accordingly, these results suggest that garnet crystals can incorporate a wide range of elements present in CMAS.

3.6.2 *Atomic-scale insights into coordination changes*

During the transformation from YbMS and YbDS to YbAG, the coordination environments of all the cations (Yb, Si, and Al) and anions (O) undergo significant changes, as indicated in Fig. 14.

First, both YbMS and YbDS have irregular and low-symmetry coordination for Yb^{3+}. YbMS has two distinct Yb sites with mixed coordination numbers (CNs) between 6 and 8, forming distorted polyhedra and octahedra, whereas YbDS typically has Yb^{3+} with 6 or 7 coordination, which is also uneven and distorted [2,12]. The YbAG structure is highly symmetric. All Yb^{3+} ions exclusively occupy dodecahedral sites and are regularly coordinated with 8 oxygen atoms. Therefore, the coordination environment of Yb is completely transformed from a mixed, irregular, low-symmetry state (CN = 6, 7, or 8) to a uniform, regular, high-symmetry dodecahedron state (CN = 8).

Second, isolated silicate units exist in the YbMS and YbDS structures, where Si^{4+} is always in 4-coordination. In YbAG, Al^{3+} replaces Si^{4+}, forming two distinct, interconnected coordination environments: $[AlO_4]$ tetrahedra (CN = 4) and $[AlO_6]$ octahedra (CN = 6) [31]. These tetrahedra and octahedra share oxygen vertices, creating a complex, continuous, and robust three-dimensional network. Therefore, the silicate structure evolves from discrete, isolated units (single or paired tetrahedra) into a continuous 3D framework of interconnected $[AlO_4]$ tetrahedra and $[AlO_6]$ octahedra. This interconnected network is a key factor in the superior stability of the YbAG structure.

Finally, the oxygen ion coordination of YbMS and YbDS is complex and nonuniform. Some oxygen atoms are bonded to 1 Si and 1-2 Yb, whereas others are connected only to 2 Yb. YbDS also has an oxygen bridging two Si atoms. The average CN is relatively low, typically 2 or 3. In the YbAG garnet structure, the oxygen coordination is highly regular such that every single O^{2-} ion is simultaneously bonded to 1 Yb (at a dodecahedral site), 1 Al (at an octahedral site) or 1 Al (at a tetrahedral site). This gives it a consistent CN of 4. Therefore, the oxygen environment changes from a complex, nonuniform, low-coordination state (CN = 2 and 3) to a perfectly uniform and regular high-coordination state (CN = 4).

In summary, the collective transformation—where all cations and anions move into highly symmetric, regular, and more interconnected coordination environments—is the fundamental reason why, compared with YbMS and YbDS, YbAG is more thermodynamically and chemically stable.

3.6.3 *Superior resistance mechanism of the aluminum-modified MS coating*

The interaction diagram of the two coatings during CMAS exposure is shown in Fig. 17. In the YbMS system, Ca-lean CMAS exhibited strong corrosion activity toward silicate components. The mobility of CMAS elements follows the order $Mg^{2+} > Ca^{2+} > Al^{3+} > Si^{4+}$ on the basis of bond strength and coordinate numbers [8]. High concentrations of Mg^{2+} and Al^{3+} promote the transformation of YbMS to garnet, leading to volume shrinkage [26]. Therefore, the garnet layer formed on the YbMS corroded surface is porous and loose (Fig. 5), making it ineffective in preventing further penetration of melt.

Additionally, the as-deposited YbMS coating contains numerous interconnected microcracks and pores, which accelerate melt penetration into the underlying layer and ultimately result in complete corrosion.

Garnet also became destabilized with the addition of MgO and SiO_2. High concentrations of Mg^{2+} and Si^{4+} attack garnet crystals, forming solid solutions that compromise their stability. This destabilization occurred as Yb^{3+} was replaced by Mg^{2+}, along with the substitution of Al^{3+} by Si^{4+}. Since SiO_2, MgO, and CaO are commonly used as sintering aids for YAG ceramics, they promote sintering by forming low-melting transient phases [32,39]. As a result, corrosive elements accumulate at the grain boundaries, lowering the melting point and accelerating the dissolution of the coating material. The composition equilibrium of the corrosion products is highly complex [18], and further investigation is needed to fully understand the CMAS corrosion mechanism of these coatings. However, these initial findings indicate that the high corrosion reactivity of YbMS coatings and increased melt penetration significantly contribute to their premature failure in CMAS environments.

The viscosity of a melt significantly affects its permeability and is strongly dependent on its oxide composition. Reducing the SiO_2 content from approximately 60 to approximately 50 mol% resulted in a decrease in the melt viscosity from 3100 to 340 poise, a reduction of nearly an order of magnitude [38]. Considering the continuous corrosion reactions and solid solution formation in the YbMS system (Reactions (4)–(6)), the consumption of SiO_2 may be even greater, which could further lower the melt viscosity, making it easier to penetrate into the coating and thus leading to deeper corrosion depths. The dense and uniform YbAG layer preformed by aluminum modification acts as a physical shield for the YbMS coating. Consequently, the consumption of SiO_2 from the melt is significantly reduced. Additionally, the Si released from YbMS during the modification (based on Reactions (1) and (3)) is subsequently oxidized to SiO_2 within the high-temperature oxygen-rich environment and dissolves into the CMAS melt, which substantially increases the viscosity of the melt. The

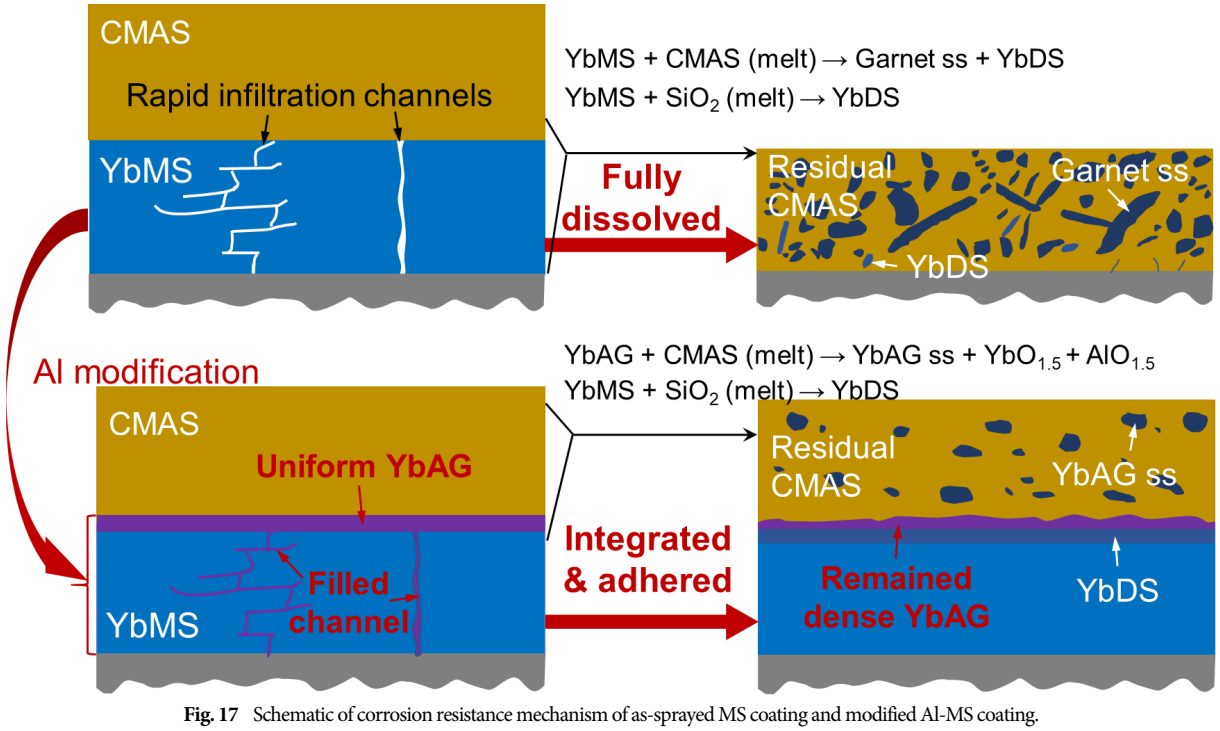

Fig. 17 Schematic of corrosion resistance mechanism of as-sprayed MS coating and modified Al-MS coating.

resulting viscous melt has drastically reduced fluidity and permeability.

Furthermore, the modification process eliminates rapid penetration pathways, such as interconnected microcracks and pores [18,21,40]. Although YbAG reacts chemically with the melt to form solid solutions and gradually dissolves, this process is highly dependent on the oxide content of the residual melt and rapidly reaches equilibrium. After 50 h of exposure, the surface YbAG layer showed only minor degradation, with the underlying structure remaining dense and continuing to provide effective protection for the YbMS coating.

4 Conclusions

An aluminum surface modification strategy was proposed to increase the CMAS corrosion resistance of YbMS coatings. The CMAS corrosion behavior and mechanisms of the as-sprayed MS and modified Al-MS coatings were systematically investigated at 1400 °C for 5, 25, and 50 h, respectively. Key findings include the following:

1) YbMS readily reacts with CMAS, forming garnet and its solid solutions, leading to complete dissolution of the coating materials within 25 h at 1400 °C, resulting in inferior corrosion resistance than that of YbDS.

2) Interconnected microcracks and pores in as-deposited coatings serve as rapid penetration pathways for CMAS, promoting deep melt infiltration and accelerating premature failure.

3) Aluminum modification effectively seals fast penetration channels and forms a uniform, stable YbAG surface layer. This barrier prevents direct YbMS-CMAS contact and increases the melt viscosity, extending the coating life by at least 10 times.

4) The lower formation energy of YbAG from YbMS, combined with its greater negative adsorption energy relative to that of YbDS, promotes a more complete reaction, which leads to the development of a highly uniform YbAG layer and, in turn, provides enhanced protection.

These findings validate aluminum surface modification as a viable strategy to improve the long-term durability of YbMS EBCs in CMAS-rich environments.

Acknowledgements

The present project is supported by the National Natural Science Foundation of China (Nos. 52301102 and 52471092), the Postdoctoral Research Foundation of China (No. 2024M752571), and the Fundamental Research Funds for the Central Universities.

Availability of data and materials

The data that support the findings of this study are available from the corresponding author upon reasonable request.

Competing interests

The authors have no competing interests to declare that are relevant to the content of this article.

References

[1] Turcer LR, Padture NP. Rare-earth pyrosilicate solid-solution environmental-barrier coating ceramics for resistance against attack by molten calcia–magnesia–aluminosilicate (CMAS) glass. *J Mater Res* 2020, **35**: 2373–2384.

[2] Zhong X, Wang YW, Liu PP, *et al.* Effects of microstructure on corrosion behaviors for RE_2SiO_5 (RE = Gd, Y, Er) environmental barrier coatings against calcium–magnesium–alumino–silicate melts. *Corros Sci* 2022, **199**: 110174.

[3] Tian ZL, Ming KY, Zheng LY, *et al. In-situ* observation and mechanism of calcium–magnesium–alumina–silicate (CMAS) melts-induced degradation of RE_2SiO_5 (RE = Tb, Dy, Ho, Y, Er, Tm, and Yb) ceramics at 1500 °C. *J Adv Ceram* 2023, **12**: 2315–2330.

[4] Zhao HB, Levi CG, Wadley HNG. Molten silicate interactions with thermal barrier coatings. *Surf Coat Tech* 2014, **251**: 74–86.

[5] Meng SJ, Guo L, Guo HB, *et al.* CMAS-phobic and infiltration-inhibiting protective layer material for thermal barrier coatings. *J Adv Ceram* 2024, **13**: 1254–1267.

[6] Han JQ, Liu MJ, Mostaghimi J, *et al.* Solid dust induced roughening and overheating of TBC-coated superalloy. *J Mater Sci Technol* 2024, **180**: 69–79.

[7] Tian ZL, Zhang J, Zheng LY, *et al.* General trend on the phase

stability and corrosion resistance of rare earth monosilicates to molten calcium–magnesium–aluminosilicate at 1300 °C. *Corros Sci* 2019, **148**: 281–292.

[8] Wu NN, Wang YL, Tong YL, *et al.* Interaction of ytterbium monosilicate environmental barrier coating material with molten calcium–magnesium–aluminosilicate (CMAS). *Corros Sci* 2023, **211**: 110864.

[9] Jang BK, Feng FJ, Suzuta K, *et al.* Corrosion behavior of volcanic ash and calcium magnesium aluminosilicate on Yb_2SiO_5 environmental barrier coatings. *J Ceram Soc Jpn* 2017, **125**: 326–332.

[10] Abrar S, Ma Z, Liu L, *et al.* Improved CMAS resistance of a newly developed high entropy ceramics monosilicate: A potential environmental barrier coating material. *Surf Coat Tech* 2023, **465**: 129618.

[11] Turcer LR, Krause AR, Garces HF, *et al.* Environmental-barrier coating ceramics for resistance against attack by molten calcia–magnesia–aluminosilicate (CMAS) glass: Part II, β-$Yb_2Si_2O_7$ and β-$Sc_2Si_2O_7$. *J Eur Ceram Soc* 2018, **38**: 3914–3924.

[12] Liu PP, Zhong X, Niu YR, *et al.* Reaction behaviors and mechanisms of tri-layer Yb_2SiO_5/$Yb_2Si_2O_7$/Si environmental barrier coatings with molten calcium–magnesium–alumino–silicate. *Corros Sci* 2022, **197**: 110069.

[13] Zhao HB, Richards BT, Levi CG, *et al.* Molten silicate reactions with plasma sprayed ytterbium silicate coatings. *Surf Coat Tech* 2016, **288**: 151–162.

[14] Stokes JL, Harder BJ, Wiesner VL, *et al.* Effects of crystal structure and cation size on molten silicate reactivity with environmental barrier coating materials. *J Am Ceram Soc* 2020, **103**: 622–634.

[15] Summers WD, Poerschke DL, Park D, *et al.* Roles of composition and temperature in silicate deposit-induced recession of yttrium disilicate. *Acta Mater* 2018, **160**: 34–46.

[16] Sternlicht H, McComb DW, Padture NP. Interaction of ytterbium pyrosilicate environmental-barrier-coating ceramics with molten calcia–magnesia–aluminosilicate glass: Part I, Microstructures. *Acta Mater* 2022, **241**: 118360.

[17] Zhao MY, Hu XX, He J, *et al.* Corrosion behavior and mechanism of ytterbium monosilicate by molten calcium–magnesium–alumino–silicate melts at 1400 and 1500 °C. *Ceram Int* 2023, **49**: 23756–23764.

[18] Harder BJ, Stokes JL, Kowalski BA, *et al.* Steam oxidation performance of $Yb_2Si_2O_7$ environmental barrier coatings exposed to CMAS. *J Eur Ceram Soc* 2024, **44**: 2486–2498.

[19] Bryce K, Majee BP, Huang LP, *et al.* A systematic study of thermomechanical properties and calcium–magnesium–aluminosilicate (CMAS) corrosion of multicomponent rare-earth phosphates. *J Adv Ceram* 2024, **13**: 1807–1822.

[20] Rose A, Gomez Chavez JJ, Mechnich P, *et al.* Novel magnetron sputtered yttrium-silicon-iron oxide as CMAS resistant top coat material for environmental barrier coatings. *Corros Sci* 2023, **215**: 111053.

[21] El Shafei K, Al Nasiri N. Corrosion behaviour of rare-earth monosilicates in CMAS exposure. *Corros Sci* 2022, **202**: 110312.

[22] Chavez JJG, Naraparaju R, Mikulla C, *et al.* Comparative study of EB-PVD gadolinium-zirconate and yttria-rich zirconia coatings performance against Fe-containing calcium–magnesium–aluminosilicate (CMAS) infiltration. *Corros Sci* 2021, **190**: 109660.

[23] Liu Y, Su HJ, Shen ZL, *et al.* High temperature calcium–magnesium–alumina–silicate (CMAS) corrosion behavior of directionally solidified Al_2O_3/YAG eutectic ceramic. *J Mater Sci Technol* 2023, **165**: 66–74.

[24] Sun HF, Sun LC, Ren XM, *et al.* Outstanding molten calcium–magnesium–aluminosilicate (CMAS) corrosion resistance of directionally solidified Al_2O_3/$Y_3Al_5O_{12}$ eutectic ceramic at 1500 °C. *Corros Sci* 2023, **220**: 111289.

[25] Dong L, Yang WQ, Chen L, *et al.* Realizing the excellent oxidation resistance of an environmental barrier coating through aluminum surface modification. *J Adv Ceram* 2024, **13**: 976–986.

[26] Dong L, Wei XW, Liu MJ, *et al.* Boosting corrosion resistance of environmental barrier coatings through surface aluminum modification against molten salts. *Corros Sci* 2025, **244**: 112646.

[27] Dong L, Liu MJ, Zhang XF, *et al.* Low temperature *in situ* formation of oxygen barriers by heat treatment of aluminum infiltrated environmental barrier coatings. *Ceram Int* 2021, **47**: 34463–34472.

[28] Luo BW, Jiang SL, Zhu WW, *et al.* Laser joining of Al_2O_3 liners with Al_2O_3–MgO–SiO_2 glass-ceramic fillers. *J Mater Process Tech* 2018, **260**: 48–56.

[29] Perrière C, Boulesteix R, Maître A, *et al.* Study of sintering mechanisms of Ca-doped yttrium aluminum garnet ceramics: From nanostructure to macroscopic behaviour. *J Eur Ceram Soc* 2023, **43**: 565–575.

[30] Lu MH, Xiang HM, Feng ZH, *et al.* Mechanical and thermal properties of Yb_2SiO_5: A promising material for T/EBCs applications. *J Am Ceram Soc* 2016, **99**: 1404–1411.

[31] Liu B, Liu YC, Zhu CH, *et al.* Advances on strategies for searching for next generation thermal barrier coating materials. *J Mater Sci Technol* 2019, **35**: 833–851.

[32] Zheng JN, Yi K, Chang CK. Intercalation of Al^{3+} into Prussian blue analogues from nonaqueous electrolytes. *Small Meth* 2025, **9**: 2401000.

[33] Poerschke DL, Shaw JH, Verma N, *et al.* Interaction of yttrium disilicate environmental barrier coatings with calcium–magnesium–iron alumino–silicate melts. *Acta Mater* 2018, **145**: 451–461.

[34] Xiao FR, Liu S, Xia J, *et al.* Corrosion of tri-layer $LaMgAl_{11}O_{19}$/Yb_2SiO_5/Si environmental barrier coatings with molten calcium–magnesium–alumina–silicate (CMAS). *Corros Sci* 2024, **227**: 111781.

[35] Wang X, Meng MY, Xu FH, *et al.* $(Lu_{1/7}Yb_{1/7}Sc_{1/7}Er_{1/7}Y_{1/7}Ho_{1/7}Dy_{1/7})_2Si_2O_7$ high entropy rare-earth disilicate with low thermal conductivity and excellent resistance to CMAS corrosion. *J Adv Ceram* 2024, **13**: 549–560.

[36] Stolzenburg F, Johnson MT, Lee KN, *et al.* The interaction of calcium–magnesium–aluminosilicate with ytterbium silicate environmental barrier materials. *Surf Coat Tech* 2015, **284**: 44–50.

[37] Vorona IO, Yavetskiy RP, Parkhomenko SV, *et al.* Effect of complex Si^{4+} + Mg^{2+} additive on sintering and properties of undoped YAG ceramics. *J Eur Ceram Soc* 2022, **42**: 6104–6109.

[38] Poerschke DL, Barth TL, Levi CG. Equilibrium relationships between thermal barrier oxides and silicate melts. *Acta Mater* 2016, **120**: 302–314.

[39] Majeed Khan MA, Nain P, Kumar S, *et al.* Improved photocatalytic and electrochemical activities of (Nd^{3+}, Yb^{3+}) co-doped TiO_2 nanoparticles synthesized by hydrothermal protocol. *J Mater Sci-Mater El* 2024, **35**: 2149.

[40] Zhong X, Wang YW, Niu YR, *et al.* Corrosion behaviors and mechanisms of ytterbium silicate environmental barrier coatings by molten calcium–magnesium–alumino–silicate melts. *Corros Sci* 2021, **191**: 109718.